



On the Evolution of a Long-Lived Mesoscale Convective Vortex that Acted as a Crucial Condition for the Extremely Strong Hourly Precipitation in Zhengzhou

Shen-Ming Fu^{1,2} , Yuan-Chun Zhang^{2,3}, Hui-Jie Wang³, Huan Tang³, Wan-Li Li⁴, and Jian-Hua Sun³ 

¹International Center for Climate and Environment Sciences, Institute of Atmospheric Physics, Chinese Academy of Sciences, Beijing, China, ²State Key Laboratory of Severe Weather, Chinese Academy of Meteorological Sciences, Beijing, China, ³Laboratory of Cloud–Precipitation Physics and Severe Storms, Institute of Atmospheric Physics, Chinese Academy of Sciences, Beijing, China, ⁴China Meteorological Administration Training Center, Beijing, China

Key Points:

- A long-lived mesoscale vortex was crucial to produce the hourly precipitation of 201.9 mm that appeared in Zhengzhou on 20 July 2021
- The extremely strong hourly precipitation appeared in the stage when the vortex interacted with its parent mesoscale convective system
- Convection-related upward and net-import horizontal transport of cyclonic vorticity dominated the vortex's development

Correspondence to:

S.-M. Fu,
fusm@mail.iap.ac.cn

Citation:

Fu, S.-M., Zhang, Y.-C., Wang, H.-J., Tang, H., Li, W.-L., & Sun, J.-H. (2022). On the evolution of a long-lived mesoscale convective vortex that acted as a crucial condition for the extremely strong hourly precipitation in Zhengzhou. *Journal of Geophysical Research: Atmospheres*, 127, e2021JD036233. <https://doi.org/10.1029/2021JD036233>

Received 22 NOV 2021
Accepted 15 MAY 2022

Author Contributions:

Conceptualization: Shen-Ming Fu
Data curation: Shen-Ming Fu, Yuan-Chun Zhang, Hui-Jie Wang
Formal analysis: Shen-Ming Fu
Funding acquisition: Shen-Ming Fu
Investigation: Shen-Ming Fu
Methodology: Shen-Ming Fu
Project Administration: Shen-Ming Fu, Jian-Hua Sun
Resources: Shen-Ming Fu, Yuan-Chun Zhang, Hui-Jie Wang
Software: Shen-Ming Fu, Yuan-Chun Zhang, Hui-Jie Wang, Huan Tang
Supervision: Shen-Ming Fu, Jian-Hua Sun
Validation: Shen-Ming Fu, Yuan-Chun Zhang
Visualization: Shen-Ming Fu, Yuan-Chun Zhang, Huan Tang, Wan-Li Li
Writing – original draft: Shen-Ming Fu, Wan-Li Li

Abstract From 17–22 July 2021, Henan Province experienced the most severe torrential rainfall event since 1975 with a maximum hourly precipitation of 201.9 mm appeared in Zhengzhou, which was the largest hourly rainfall thus far observed by meteorological observation stations over the Chinese Mainland. The appearance of a long-lived (21-hr) northwestward-moving mesoscale convective vortex (MCV) and its interaction with its parent mesoscale convective system (MCS) was crucial to produce the extremely strong heavy rainfall in Zhengzhou. The backward trajectory analysis indicates that air particles in the lower troposphere beneath the MCS over Henan contributed mostly to the MCV's formation. These air particles experienced notable ascending motions and condensation with their strong cyclonic vorticity mostly produced 1-hr before the MCV's formation. Vorticity budget denotes that strong upward transport of cyclonic vorticity and convergence-related vertical stretching, both of which were mainly due to convection associated with the parent MCS, acted as dominant factors for the MCV's formation. After formation, the MCV first coupled with its parent MCS, during which its intensity, thickness, and precipitation were all maximized; then, it moved northwestward and decoupled from the MCS, during which it weakened rapidly and finally dissipated. Convection-related upward cyclonic vorticity transport and inward horizontal advection of cyclonic vorticity associated with an inverted trough over the Henan Province dominated the vortex's development/maintenance in the coupling stage; whereas outward horizontal advection of cyclonic vorticity dominated the MCV's dissipation after it completely decoupled from its parent MCS. These differ notably from the findings documented in previous MCV-related literature.

1. Introduction

Torrential rainfall is one of the most severe natural disasters in China, which causes severe economic losses and heavy casualties every year (Song, 2018; Zhao et al., 2004). North China is a major rainfall region for the east of China (Tao, 1980) with most of its rainstorms appeared in the period from late July to early August. Of these, the “58.7” (14–19 July 1958; the middle reaches of the Yellow River Basin) torrential rainfall event (TRE), “63.8” TRE (1–9 August 1963; Hebei Province), “75.8” TRE (5–7 August 1975; Henan Province), and “7.21” TRE (21–22 July 2012; Beijing) were all famous for their extreme intensity and catastrophic destructive power. Most recently, a TRE appeared in Henan Province, which broke a series of historical records in China (Yin et al., 2022). This rainfall event lasted for a total of ~6 days (from 17 to 22 July 2021; it was named as the “21.7” TRE in China), killed over 300 people, destroyed a harvest area of ~1800000 ha, damaged ~190000 houses, caused an electricity blackout of ~3740000 households, and resulted in a direct economic loss of up to ~114 billion Yuan.

The most striking feature of the “21.7” TRE is that an hourly precipitation of 201.9 mm appeared in Zhengzhou (the capital of Henan Province). This is the largest hourly precipitation that had been observed by meteorological observation stations over the Chinese Mainland. Henan Province is located between the Huang River and Yangtze River (Figure 1a) with mountains above 1000 m mainly located in its western section. In terms of mean state of strong hourly precipitation (≥ 15 mm), regions northeast of Henan were heavier than that of Henan, whereas other regions surrounding Henan were mainly lighter. Within Henan, stronger precipitation tended to appear along the Huang River and in its eastern section, and the Zhengzhou station (small green box in Figure 1a) had a mean hourly precipitation of below 25 mm (not the largest one in this region). In terms of maximum hourly

Writing – review & editing: Shen-Ming Fu

precipitation (Figure 1b), except for the regions northwest and west of Henan, Henan did not experience notably stronger hourly rainfall than its surrounding regions, and Zhengzhou only had a maximum hourly precipitation of below 100 mm during the warm seasons (May–September) of 1981–2020. As shown in Figure 1c, for the Zhengzhou station, the hourly precipitation of 201.9 mm was larger than the second maximum value by ~110 mm and stronger than the median value by ~180 mm. According to statistical analyses mentioned above, it seems that the Zhengzhou station did not show notably distinctive features from other stations in Henan to guarantee that it experienced stronger hourly rainfall than those of other stations. Therefore, the extremely strong hourly rainfall was an accidental event for Zhengzhou.

The extremely strong hourly rainfall of Zhengzhou was induced by combined factors (Yin et al., 2022) with a long-lived mesoscale convective vortex (MCV) being one of the key reasons. In China, meso- α -scale (200–2,000 km; Orlanski, 1975) vortices are active in summer, of which the Tibetan Plateau vortices (TPV; Curio et al., 2018, 2019; X. Feng et al., 2014; Fu et al., 2019; Yu & Gao, 2006), southwest vortices (SWV; S.-L. Feng et al., 2019; Ni et al., 2017), and Dabie vortices (DBV; Fu et al., 2016; Yang et al., 2010; J.-P. Zhang et al., 2015) show the largest occurrence frequency. However, for MCVs (https://glossary.ametsoc.org/wiki/Mesoscale_convective_vortex), their frequency is much less than these three types of vortices (X. Feng et al., 2014; Fu et al., 2015, 2016). Moreover, the occurrence frequency of MCVs is also much less than that of mesoscale convective systems (MCSs; Bartels & Maddox, 1991; James & Johnson, 2010; Surowiecki & Taszarek, 2020). Compared to TPVs, SWVs, and DBVs, which have been widely investigated in China, the MCVs usually have a smaller horizontal size but a larger cyclonic vorticity and a closer relationship to the MCSs. All these features indicate that understandings about the widely investigated TPVs, SWVs, and DBVs cannot be directly extended to MCVs. Since there are only a few studies on the MCVs in China, it is necessary to carry out specialized research studies on this topic. Moreover, a brief comparison between the MCV in China and that in North America is also useful to render a more comprehensive understanding of this type of vortex. As a result, the primary purpose of this study is to explore key features of the MCV that acted as a crucial condition for the extreme hourly rainfall in Zhengzhou and to understand the mechanisms governing its formation and evolution. The remainder of this article is structured as follows: Data and methods are presented in Section 2, an overview of the rainfall event is shown in Section 3, key features of the MCV and the mechanisms governing its formation and evolution are discussed in Sections 4 and 5, respectively, and finally, the conclusion and discussion are provided in Section 6.

2. Data and Method

2.1. Data

Overall, three types of data were used in this study: (a) the hourly precipitation observations at meteorological stations from the China Meteorological Administration were used to analyze the precipitation in Henan Province; (b) the hourly, $0.25^\circ \times 0.25^\circ$ ERA5 reanalysis data (with 37 vertical levels) provided by the European Centre for Medium Range Weather Forecasts (Hersbach et al., 2020) were used for synoptic analyses, quantitative calculations, and backward tracking; and (c) the temperature of black body (TBB) from the Fengyun (FY)-IV satellite with a temporal resolution of hourly and a spatial resolution of $0.05^\circ \times 0.05^\circ$ (<http://satellite.nsmc.org.cn/Portal-Site/Data/Satellite.aspx>) was used for analyses of MCSs.

2.2. Method

This study regarded a closed counterclockwise circulation in the stream field coupled with a cyclonic vorticity center $\geq 10^{-5} \text{ s}^{-1}$ as a vortex structure (Fu et al., 2016). The vertical extent (i.e., thickness) of a vortex was determined by checking all continuous vertical levels for the occurrence of notable vortex structures that belonged to the same vortex. With the vertical extent of a vortex, the vertical level with the largest pressure was defined as the bottom level of the vortex, and that with the smallest pressure was defined as the top level of the vortex. The definition of an MCS from Mai et al. (2020) was used in this study: (a) the MCS's cloud area with TBB $\leq -52^\circ\text{C}$ must exceed 5,000 km² and (b) the condition (a) must be satisfied for at least three consecutive hours.

The HYSPLIT model (Stein et al., 2015) was used in this study for tracking air particles that formed the long-lived MCV during the “21.7” TRE. The backward tracking was initiated at 2200 UTC 19 July, when the MCV formed, and ended at the time 24-hr before the MCV's formation. A total of 567 air particles, which were located

evenly at 7 vertical levels (750 hPa, 725 hPa, 700 hPa, 675 hPa, 650 hPa, 625 hPa, and 600 hPa; the MCV was located at the layer of 750–600 hPa when it formed), were used in the backward tracking. At each vertical level, there were 81 dots, which were distributed evenly (i.e., in a spatial resolution of $0.25^\circ \times 0.25^\circ$) within a box of the size of $2^\circ \times 2^\circ$ centered at the vortex's center. This box was determined by the temporal mean of the MCV's size and was named as the key region of the vortex. Sensitivity tests, which modified each boundary line of the key region by $\pm 0.25^\circ$, showed that key-region averaged features (including vorticity budget) were insensitive to these relatively small changes. This means that the selection of the key region was representative.

According to the Green's theorem (i.e., the surface integral of vorticity within an area equals the velocity of circulation along the boundary line of this region), the horizontal averaged vorticity can effectively represent the variation of a vortex (Fu et al., 2017). Therefore, we used the vorticity budget (Kirk, 2003) to analyze the MCV's formation and evolution. The expression is:

$$\frac{\partial \zeta}{\partial t} = -\mathbf{V}_h \cdot \nabla_h \zeta - \omega \frac{\partial \zeta}{\partial p} - \beta v - (\zeta + f) \nabla_h \cdot \mathbf{V}_h + \mathbf{k} \cdot \left(\frac{\partial \mathbf{V}_h}{\partial p} \times \nabla_h \omega \right) + \text{RES} \quad (1)$$

where \mathbf{i} , \mathbf{j} , and \mathbf{k} are the unit vectors in the zonal, meridional, and zenith directions, respectively. (u , v , and ω) are the zonal, meridional, and vertical winds in the pressure coordinate, respectively. ζ is the relative vorticity in the \mathbf{k} direction (vorticity, hereinafter the same), t is time, $\mathbf{V}_h = u\mathbf{i} + v\mathbf{j}$ is the horizontal wind vector, $\nabla_h = \frac{\partial}{\partial x}\mathbf{i} + \frac{\partial}{\partial y}\mathbf{j}$ is the horizontal gradient operator, and $\beta = \frac{\partial f}{\partial y}$, where f is the Coriolis parameter. The term on the left-hand side of Equation 1 is the local time derivative of vorticity; the first and second terms on the right-hand side of Equation 1 are the horizontal and vertical advectons of vorticity (HAV and VAV for short), respectively; the third term is the advection of planet vorticity (APV); the fourth term denotes the stretching effect (STR); the fifth term represents the tilting effect (TIL), and the last term stands for the residual effect (mainly due to friction, subgrid effect, calculation errors, etc.). The total effect term (TOT) is defined as $\text{TOT} = \text{HAV} + \text{VAV} + \text{APV} + \text{STR} + \text{TIL}$, which stands for the total effect of all right-hand-side terms of Equation 1 except for RES. Before the analysis, we compared $\frac{\partial \zeta}{\partial t}$ with TOT (by a ratio of $\frac{\partial \zeta}{\partial t} / \text{TOT}$) and found that the ratio was mainly between 0.72 and 1.08 with a mean value of 0.79 (not shown). This means that the vorticity budget equation was mainly in a quasi-balanced state, which could be used for further analyses.

3. Overview of the Rainfall Event

Overall, the “21.7” TRE in Henan lasted from 17–22 July 2021, during which an accumulated precipitation of 993.1 mm appeared in Zhengzhou (Sun et al., 2021). The temporal distribution of precipitation during the 6-d period was not even with stronger rainfall mainly occurred on 19 and 20, July (Figure 2). One of the most distinct features during this period is that a northward-moving MCV controlled Henan Province (Figure 2a), which produced heavy precipitation east of the vortex. The MCV formed at 2200 UTC on 19 July in the western section of Henan, then moved northwestward with time, and finally dissipated at 1900 UTC on 20 July in the region ~ 200 km northwest of Henan. During its 21-hr life span, two notable hourly precipitation peaks appeared (Figure 2b), one was 201.9 mm (from 0800 UTC to 0900 UTC 20 July) at the Zhengzhou station (ID 57083), ~ 150 km east of the MCV (see the orange circle and orange pentagram in Figure 2a), and the other was 103.4 mm (from 1300 UTC to 1400 UTC 20 July) at the Kaifeng station (ID 57091), ~ 300 km east of the MCV. Moreover, 2-hr after the MCV's dissipation, a new rainfall peak of 113.9 mm appeared, which was not related to the MCV.

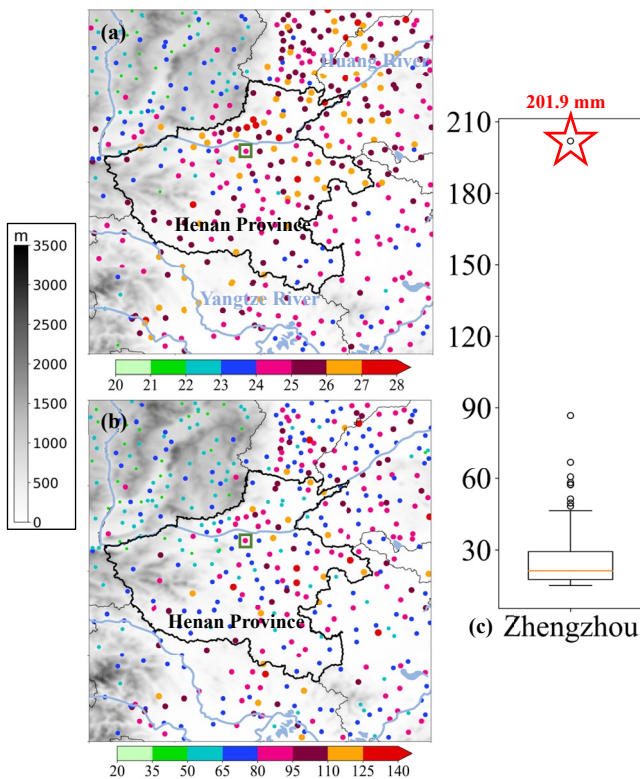


Figure 1. Panel (a) shows the average hourly precipitation (≥ 15 mm; shading dots; mm) during the warm seasons (May–September) of 1981–2020, where the small green box marks the location of the Zhengzhou station and gray shading represents terrain (m). Panel (b) is the same as panel (a), but for the maximum hourly precipitation at each station during the warm seasons of 1981–2020. Panel (c) is the box whisker diagram of hourly precipitation at Zhengzhou station (mm) from May 1980 to July 2021. The box shows the 25th (Q1)–75th (Q3) percentiles, the red line marks the median value, the whiskers indicate the range of $[Q1 - 1.5 \times (Q3 - Q1)]$ (or the minimum of the data) and $[Q3 + 1.5 \times (Q3 - Q1)]$ (or the maximum of the data), the small black hollow circles are values beyond the upper whisker, and the red pentagram marks the extremely strong hourly precipitation during the “21.7” torrential rainfall event.

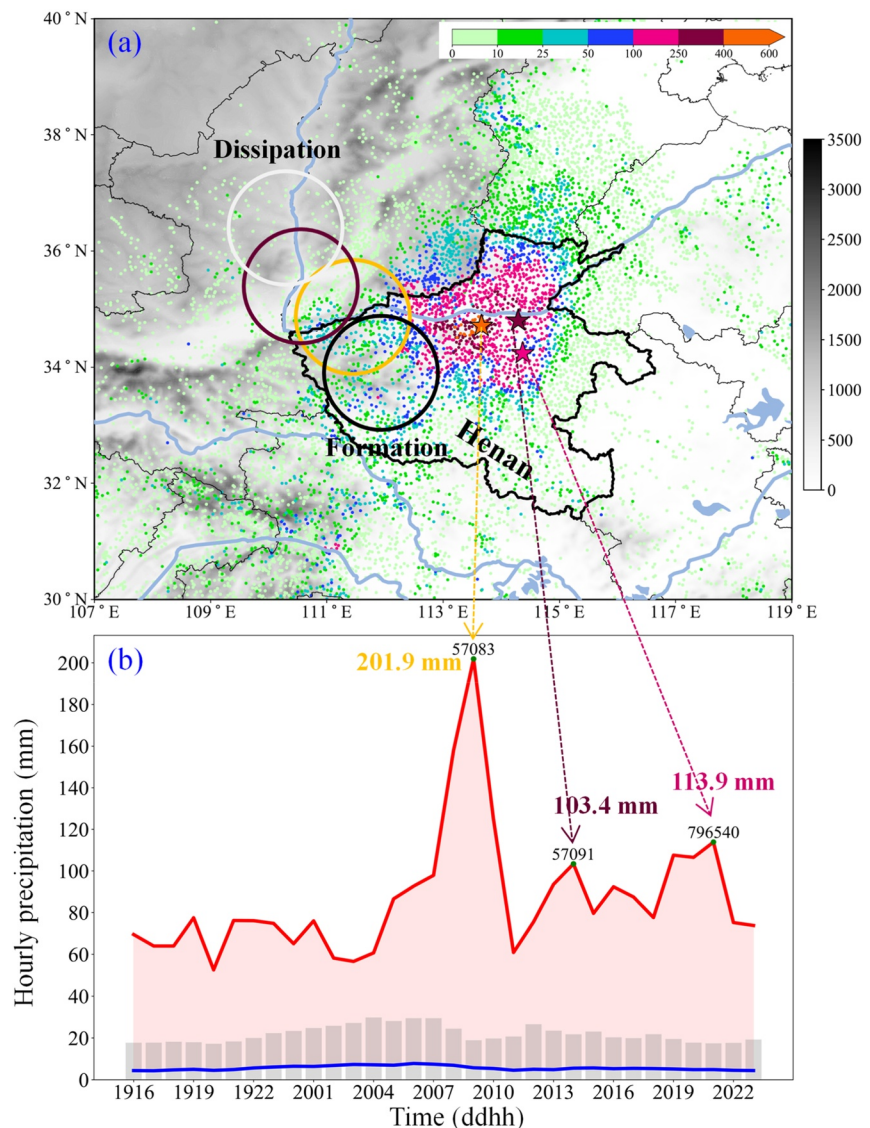


Figure 2. Panel (a) shows the 21-hr (from 2200 UTC 19 to 1900 UTC 20 July 2021) accumulated precipitation (shading dots; mm), where pentagrams mark the three stations (their IDs are 57083 = Zhengzhou, 57091 = Kaifeng, and 796540, respectively) with the maximum hourly precipitation appeared. Orange and dark red circles show the central regions of the mesoscale convective vortex (MCV) (radius of the vortex is ~ 100 km) when the maximum hourly precipitation appeared at stations 57083 and 57091, respectively; black and gray circles outline the central regions of the MCV when it is formed and dissipated, respectively. Panel (b) shows the variation of hourly precipitation at stations in Henan from 1600 UTC 19 to 2200 UTC 20 July 2021, where the red and blue lines represent the maximum value and average value, respectively. The gray bar shows the 95th quantiles of all stations in Henan at each hour.

4. Overview of the MCV

4.1. Background Environment

During the MCV's life span, in the upper troposphere, Henan and the region north of it (i.e., the regions where the MCV passed) were dominated by strong divergence (Figure 3a), which was located ahead of a 200-hPa shortwave trough. Different from the statistical results from James and Johnson (2010), this divergence was not associated with an upper-level jet streak. Strong upper-level divergence was favorable for maintaining ascending motions at lower levels due to fluid continuity. In the middle troposphere, Henan and the region north of it were governed by notable warm advection (Figure 3b) that was located in the eastern section of a 500-hPa inverted trough. Middle-level warm advection contributed to ascending motions due to quasi-geostrophic forcing (Holton, 2004).

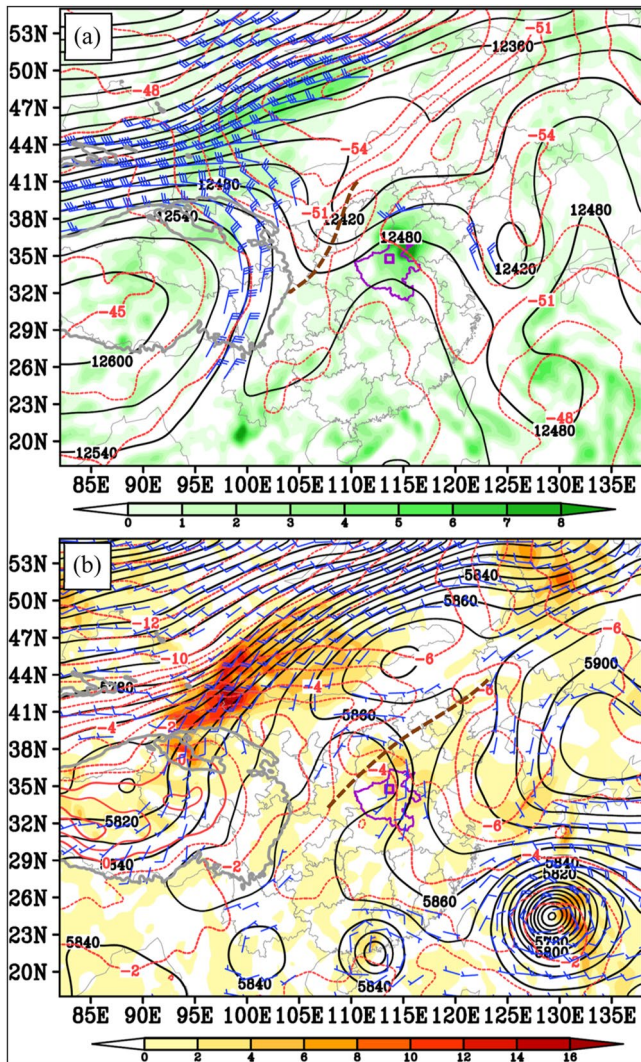


Figure 3. Panel (a) shows the temporal average (from 2200 UTC 19 to 1900 UTC 20, July) of divergence (shading; 10^{-5} s^{-1}), geopotential height (black contour; gpm), temperature (red contour; K), and wind above 25 m s^{-1} (a full bar is 10 m s^{-1}) at 200 hPa, where the brown-dashed line is the trough line. Panel (b) shows the temporal average of temperature advection (shading; 10^{-5} K s^{-1}), geopotential height (black contour; gpm), temperature (red contour; K), and wind above 5 m s^{-1} (a full bar is 10 m s^{-1}) at 500 hPa, where the brown-dashed line is the trough line.

Moreover, Henan and the region north of it were mainly controlled by middle-level southerly and southeasterly winds, which steered the MCV to move northwestward.

4.2. Variations of the MCV

The MCV is formed at 2200 UTC 19 July (Figure 4a) mainly within the stratiform region of the MCS that covered Henan. This MCS was its parent MCS. At this time, the vortex was located in the layer of 750–600 hPa (Figure 5a), which was characterized by a strong cyclonic vorticity and a weak southeasterly wind. Intense divergence governed the lower layer (750–650 hPa) of the vortex, and strong convergence controlled its upper layer (Figure 5b). This is different from the typical vertical configuration associated with SWVs and DBVs, which was characterized by lower-layer convergence and upper-layer divergence (Fu et al., 2017; Ni et al., 2017). Strong positive potential vorticity (PV) appeared in the eastern section of the MCV (Figure 6a), where ascending motions were strong. The strong positive PV was mainly due to the precipitation-related latent heat release associated with the MCS. Over the MCV (450–200 hPa), a strong ($\geq 2 \text{ K}$) positive temperature deviation (relative to the zonal mean from 105°E to 120°E) appeared due to latent heating, which was a typical feature for an MCV (James & Johnson, 2010; Trier & Davis, 2007).

After formation, the MCV's evolution can be roughly divided into two stages: during Stage I (2200 UTC 19–1200 UTC 20, July), the MCV mainly coupled with the MCS over Henan and maintained strong intensity (Figures 4a–4f); in Stage II (1200 UTC–1900 UTC 20, July), the MCV completely decoupled from its parent MCS (Figures 4g and 4h) and dissipated rapidly. Stage I can be further divided into three periods. Period I: from 2200 UTC 19 to 0000 UTC 20 July, the MCV mainly weakened in cyclonic vorticity and ascending motions (Figures 5a and 5b), consistent with the weakening of the MCS within the key region (cf., shading areas within the purple boxes shown in Figures 4a and 4b). In this period, the upper and lower layers of the MCV were governed by strong convergence and divergence, respectively (Figure 5b), which were detrimental for ascending motions. Period II: from 0000 UTC to 0900 UTC 20, July, the MCV first enhanced in cyclonic vorticity and ascending motions and then maintained the both in strong intensity (Figures 5a and 5b). In this period, the upper and lower layers of the MCV were dominated by intense divergence and convergence, respectively (Figure 5b), which contributed to sustaining ascending motions. Positive PV and positive temperature deviation within the MCV's vertical extent became stronger than those in Period I (cf., Figures 6a and 6b), implying that precipitation-related latent heating was enhanced. The Zhengzhou station was mainly located in the ascending motions associated with the MCV (Figures 6b and 6c) with its precipitation enhancing finally to the value of 201.9 mm (thick blue line in Figure 5c). It should be noted that the intensification of southerly wind (at 700–650 hPa above Zhengzhou) associated with the MCV (Figures 4e and 5c) enhanced convergence, which was also favorable for the heavy rainfall. Period III: from 0900 UTC to 1200 UTC 20, July, as moving northwestward, the MCV began to decouple from its parent MCS and weakened both in cyclonic vorticity and ascending motions (Figures 5a and 5b). In this period, divergence dominated the vertical extent of the vortex (Figure 5b), and precipitation at the Zhengzhou station decreased rapidly (Figure 5c).

The vertical extent of the MCV varied with time with the thickest value of 800–475 hPa ($\sim 3.2 \text{ km}$) appeared at 0200 UTC 20 July (thick purple lines in Figure 5a) and the thinnest value of 25 hPa appeared in Stage II (Figure 6a). Overall, the vortex's vertical extent was much thicker when it coupled with its parent MCS than that after it decoupled from the MCS (Figure 5a). This was consistent with the contrast of precipitation and intensity

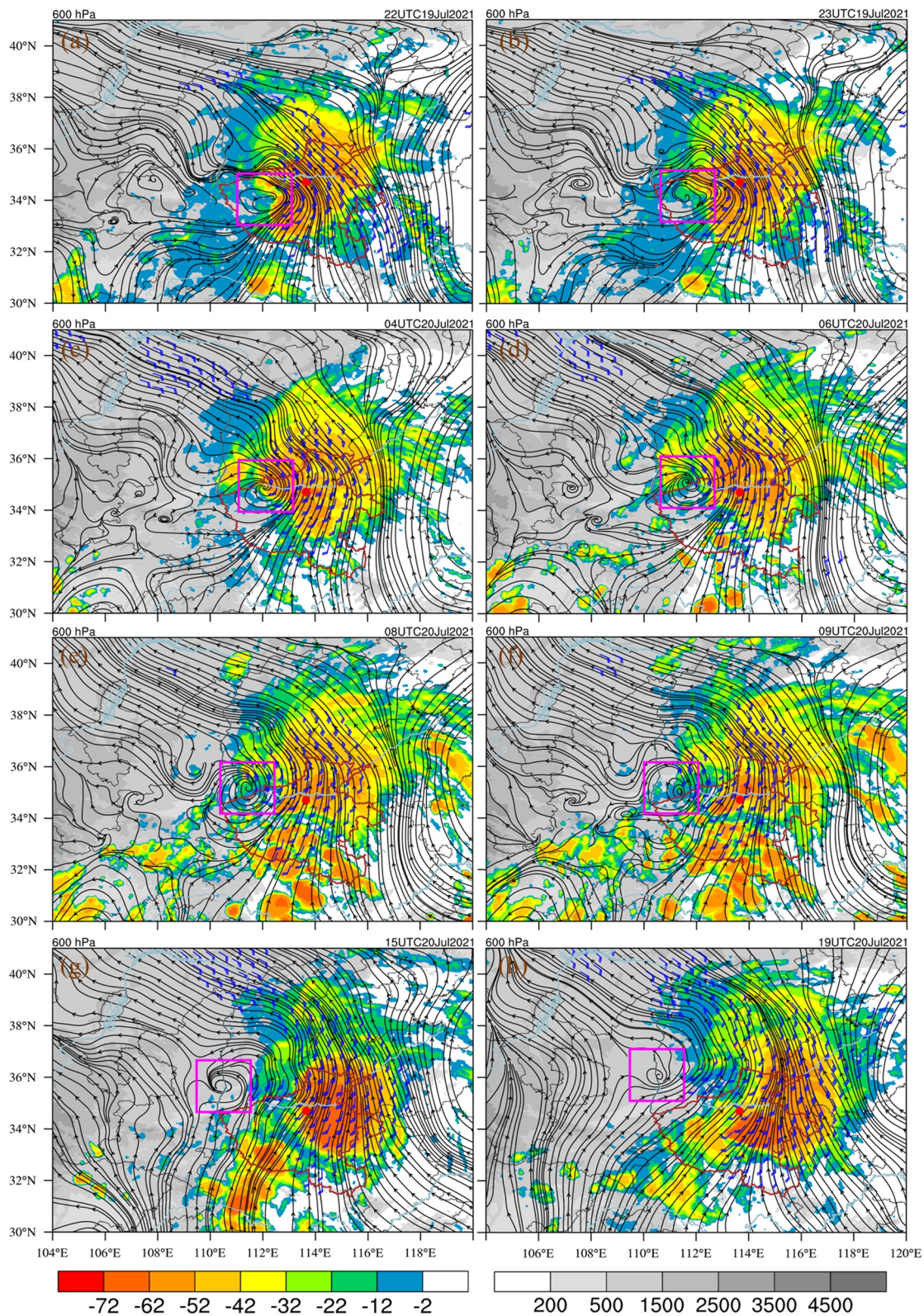


Figure 4. Temperature of black body (shading; K), stream field (black lines with arrows), and wind above 8 m s^{-1} (a full bar is 4 m s^{-1}) at 600 hPa, where the gray shading represents terrain (m), red dots mark the location of Zhengzhou, and purple boxes mark the mesoscale convective vortex's key regions.

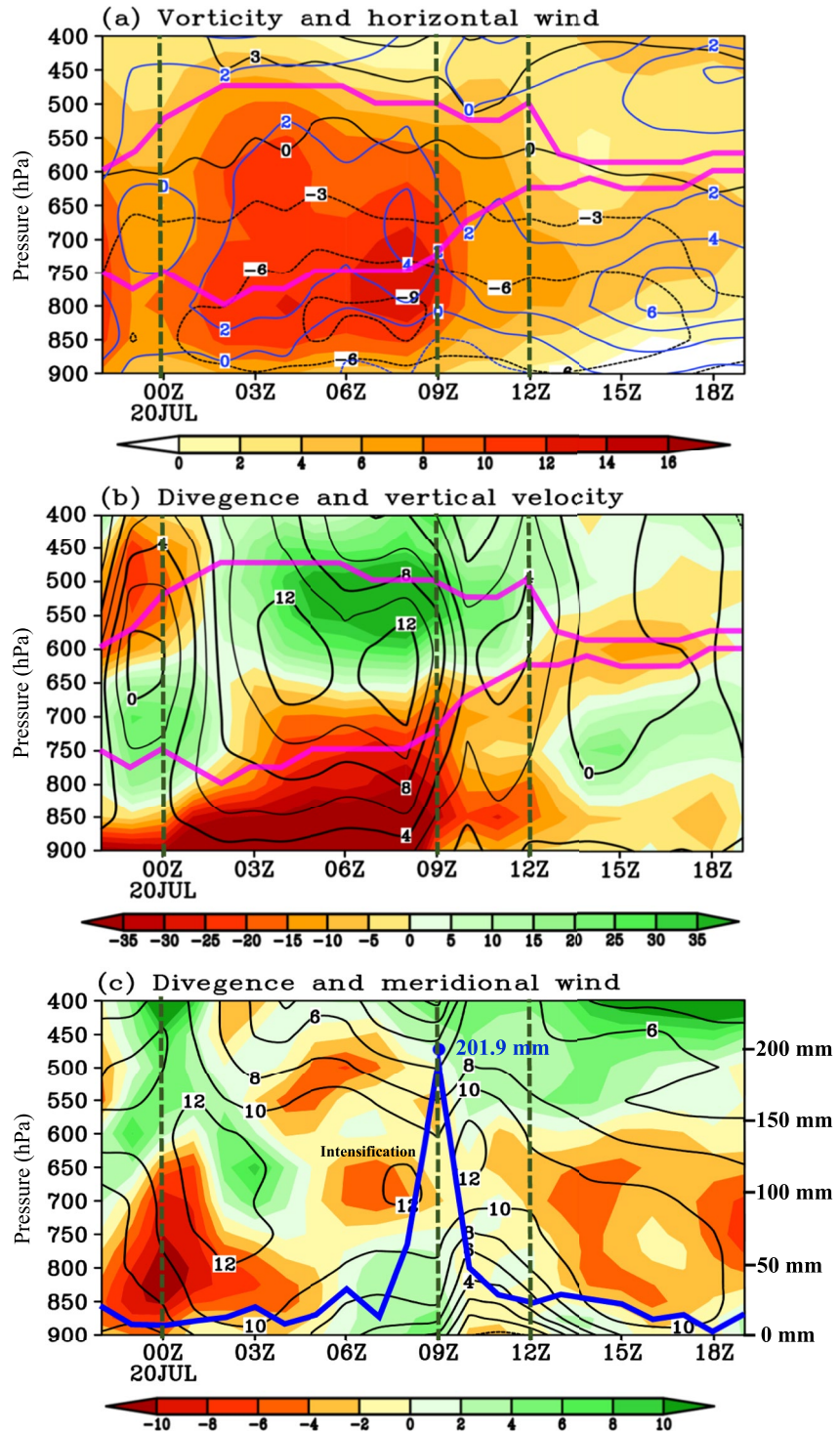


Figure 5. Panel (a) shows the key-region averaged vorticity (shading; 10^{-5} s^{-1}), zonal wind (black contour; m s^{-1}), and meridional wind (blue contour; m s^{-1}). Panel (b) shows the key-region averaged divergence (shading; 10^{-6} s^{-1}) and ascending motions (black contour; cm s^{-1}). Thick purple lines are the top and bottom levels of the mesoscale convective vortex (MCV), respectively. Panel (c) shows the horizontal average (within a $0.5^\circ \times 0.5^\circ$ box centered in the Zhengzhou station) divergence (shading; 10^{-5} s^{-1}) and meridional wind (black contour; m s^{-1}) as well as hourly precipitation at the Zhengzhou station (thick blue line; mm). Thick dashed green lines mark typical stages of the MCV.

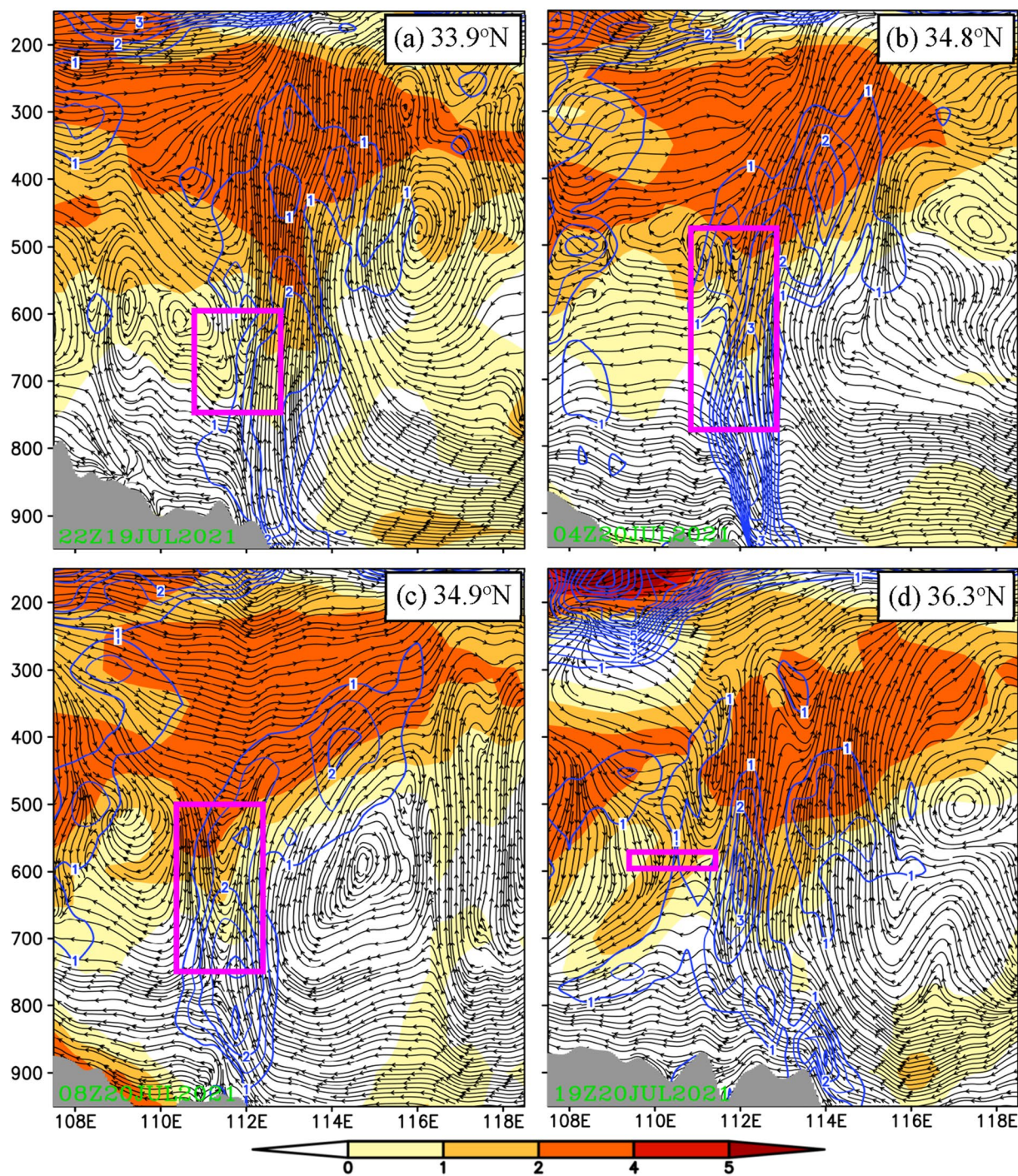


Figure 6. Cross sections through central latitudes of the mesoscale convective vortex (MCV): (a) 33.9°N, (b) 34.8°N, (c) 34.9°N, and (d) 36.3°N, where shading is temperature deviation (K), stream lines are composed by zonal wind (m s^{-1}) and vertical wind (cm s^{-1}), blue contours are potential vorticity (PVU; $1 \text{ PVU} = 10^{-6} \text{ K m}^{-2} \text{ kg}^{-1} \text{ s}^{-1}$), gray shading at the bottom represents terrain, purple rectangles outline the vertical extent of the mesoscale convective vortex, and the green bars in panels (b and c) show the location of Zhengzhou station.

(in terms of cyclonic vorticity and ascending motions) of the vortex. The largest thickness of the MCV appeared in Period II (mean thickness was $\sim 2.7 \text{ km}$), during which the Zhengzhou station experienced the extremely hourly rainfall of 201.9 mm.

4.3. Contribution of the MCV to the Heavy Rainfall in Zhengzhou

From Figure 2a, after the MCV's formation, strong precipitation appeared in Henan. From 2200 UTC 19 (i.e., vortex formation) to 0800 UTC 20 July, regions east of the vortex were governed by a strong wind zone, which changed slowly in range and intensity (Figures 4a–4e); and then from 09 UTC to 19 UTC July, following the rapid intensification of the MCV's parent MCS, the strong wind zone developed notably (Figures 4f–4h). In the period of 0800 UTC–0900 UTC 20 July, the maximum hourly precipitation of 201.9 mm appeared at the Zhengzhou station. In this period, the Zhengzhou station was situated ~250 km east of the MCV's center (Figure 4e), which was controlled by strong MCV-associated southerly wind ($\geq 8 \text{ m s}^{-1}$). Mainly due to the mountain drag effect (Carissimo et al., 1988; Tuti, 1991), the southerly wind decelerated in the region immediately south of the mountain around 37°N (Figure 2a). This resulted in convergence in the lower section of the MCV's vertical extent (Figure 5b), which contributed to ascending motions due to fluid continuity. As the atmosphere was nearly saturated in the lower and middle troposphere (not shown), strong ascending motions induced heavy precipitation, which resulted in notable latent heat release. This could be reflected by a strong positive temperature deviation and a notable PV center of ≥ 1.5 PVU (Figure 6c) in the middle and upper troposphere. Latent heating in turn promoted the ascending motions and the lower-level convergence, forming a positive feedback that enhanced all the three notably (Fu et al., 2017; Raymond & Jiang, 1990). This was one of the key factors that contributed to the occurrence of the extremely heavy precipitation at the Zhengzhou station.

5. Mechanisms Governing the MCV's Formation and Evolution

5.1. Formation Mechanisms

5.1.1. Backward-Tracking Analyses

As discussed in Section 3, the MCV formed at 2200 UTC 19 July 2021, and its vertical extent was from 750 hPa to 600 hPa. A 24-hr backward tracking analysis was conducted based on this (Section 2.2). We first classified the air particles into two categories: Type I: those had cyclonic vorticity at the time when the MCV formed, which accounted for ~98.8% of all 576 air particles (Figure 7a). These air particles were regarded as favorable for the MCV's formation. Type II: those had anticyclonic vorticity at the time when the MCV formed (~1.2% in contribution), which was regarded as detrimental for the vortex's formation. For Type II, air particles all came from the lower layer (Table 1; typically, 750 hPa is around 2,500 m and 600 hPa is around 4,000 m. Therefore, relative to the MCV's vertical extent, the higher layer means the layer higher than the top level of the vortex, so it is the layer above 4,000 m; middle layer means the layer same to the vortex's vertical extent, so it is the layer of 2,500–4,000 m; and the lower layer means the layer lower than the bottom level of the MCV, so it is the layer below 2,500 m.); for Type I, air particles came from the lower layer contributed the largest (~76.2%), and those from the middle layer were also important (~21%), but those from the upper layer occupied the smallest proportion (~1.6%). Further analysis indicates that ~61.8% of all air particles were originated from the lower layer, which was located in the region east of the MCV (Table 1). These air particles were directly related to the parent MCS that covered Henan (Figure 4). In addition, ~18.4% of all air particles came from the middle layer, which was located in the region southwest of the vortex (Table 1). They made the second contribution.

Air particles originated from the lower layer showed notable ascending motions (from a mean height of ~1,100 m–~3,200 m) during 24-hr before the MCV's formation (Figure 7k). They experienced a remarkable decrease in specific humidity and an increase in potential temperature (Figures 7e and 7h), implying that precipitation and associated latent heating were strong. The air particles that originated from the middle layer mainly showed weak ascending motions (Figure 7j) and those from the upper layer only experienced slight descending motions (Figure 7i). Specific humidity (Figures 7c and 7d) and potential temperature (Figures 7f and 7g) of these two types of air particles did not change obviously, implying that condensation and evaporation associated with them were weak. From Figures 7l–7n, it is clear that all Type-I air particles experienced notable enhancement in their cyclonic vorticity. Overall, the air particles originated from the lower layer, middle layer, and upper layer enhanced their respective mean vorticity (the value was calculated by the mean vorticity of a kind of air particles at the time when the MCV formed minus the mean vorticity at the time of 24 hr before the vortex's formation) by $\sim 17 \times 10^{-5} \text{ s}^{-1}$, $\sim 12 \times 10^{-5} \text{ s}^{-1}$, and $\sim 5 \times 10^{-5} \text{ s}^{-1}$, with those from the middle layer changed from anticyclonic vorticity (around $-1 \times 10^{-5} \text{ s}^{-1}$) to cyclonic vorticity ($\sim 11 \times 10^{-5} \text{ s}^{-1}$) and those from the lower layer changed from moderately ($\sim 3 \times 10^{-5} \text{ s}^{-1}$) to intensely cyclonic vorticity ($\sim 20 \times 10^{-5} \text{ s}^{-1}$). Notable

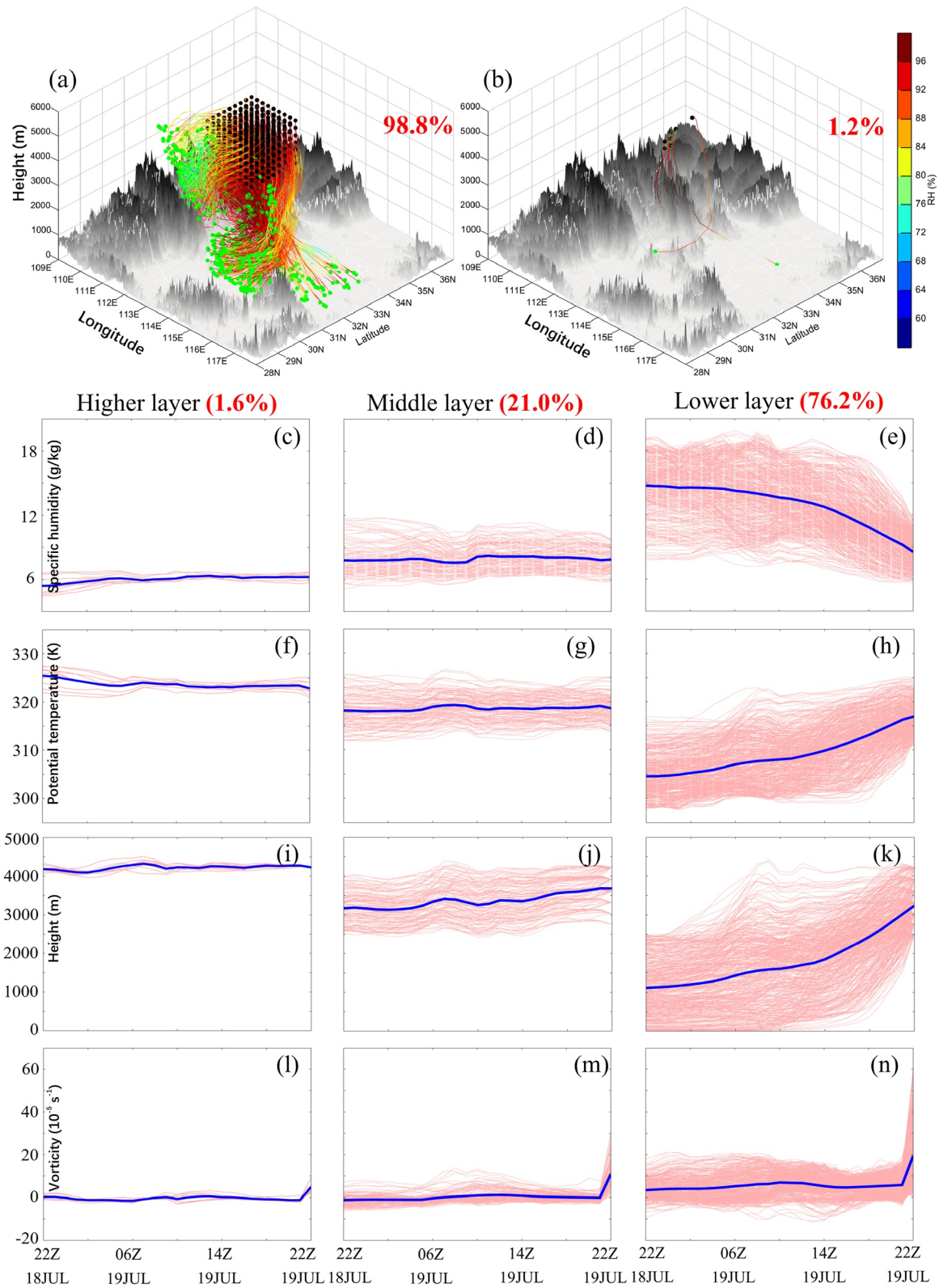


Figure 7.

Table 1

Proportion of the Air Particles That Formed the Mesoscale Convective Vortex (MCV) at 2200 UTC 19 July (i.e., the Formation Time), Where “Negative” and “Positive” Mean That the Air Particles had Anticyclonic and Cyclonic Vorticity When the MCV Formed, Respectively; “All” Means All Air Particles in the “Positive” Category; “EA” Means Air Particles Came From Regions East of the Key-Region’s Eastern Boundary Line; and “SW” Means Air Particles Came From Regions South of the Key-Region’s Southern Boundary Line and West of the Key-Region’s Eastern Boundary Line

		Higher layer (higher than 4,000 m)	Middle layer (2,500– 4,000 m)	Lower layer (lower than 2,500 m)
Negative (1.2%)		0.0%	0.0%	1.2%
Positive (98.8%)	All	1.6%	21.0%	76.2%
	EA	0.0%	1.9%	61.8%
	SW	1.6%	18.4%	10.1%

Note. All proportions were calculated relative to the total number of all air particles (i.e., 576).

enhancement of cyclonic vorticity of all Type-I air particles only appeared in the last hour of the backward tracking (i.e., from 2100 UTC to 2200 UTC 19 July), whereas in other 23 hr, their vorticity changed slightly. This means that the period from 2100 UTC to 2200 UTC 19 July was the key stage for the MCV’s formation.

5.1.2. Key-Region Averaged Features

As discussed above, the analyses based on the Lagrangian viewpoint determined the key stage for the MCV’s formation. This section analyzed the vortex’s formation from the viewpoint of Euler. The purple box in Figure 4a shows the key region of the MCV at the time when it is formed. Using it, we analyzed the key-region averaged basic features and a vorticity budget of 600 hPa (as shown in Figure 5a, the MCV had a notable vortex structure at 600 hPa throughout its life span) and the vertical mean from 750 hPa to 600 hPa (i.e., the MCV’s vertical extent). As shown in Figures 8a and 8b, from 2100 UTC to 2200 UTC 19 July (before formation), the key region also experienced rapid enhancement in cyclonic vorticity corresponding to the MCV’s formation. At this key stage, the MCV’s key region was covered by its parent MCS over Henan (Figures 8g and 8h), and precipitation was strong within it (Figures 8e and 8f). Due to convection and associated latent heating, both convergence (particularly around 600 hPa) and positive PV enhanced within the key region. These were favorable for the MCV’s formation.

From Figures 8c and 8d, term TOT enhanced notably from 2100 UTC to 2200 UTC 19 July, which was mainly due to the strong upward transport of cyclonic vorticity (i.e., VAV) and the convergence-related vertical stretching (i.e., STR). By comparison, term VAV, which was due to convective activities, was the dominant factor for the rapid increase of cyclonic vorticity during this period, and term STR, which was also closely related to convection, acted as the second dominant factor (it was ~40% of VAV at 600 hPa and ~64% of VAV within the MCV’s vertical extent). In contrast, tilting effect (i.e., TIL) and net-export horizontal transport of cyclonic vorticity from the key region (i.e., HAV) mainly decelerated the MCV’s formation. As discussed above, the formation of the MCV was mainly a result of convection. In addition, the comparison between the horizontal processes (HAV + STR) and vertical processes (VAV + TIL) showed that the latter dominated the increase in cyclonic vorticity from 2000 UTC to 2100 UTC 19 July, whereas the former dominated the vorticity increase from 2100 UTC to 2200 UTC 19 July (Figures 8c and 8d).

5.2. Evolutionary Mechanisms

During Period I (from 2200 UTC 19 to 0000 UTC 20 July), term TOT was negative (Figure 9a), corresponding to the MCV’s weakening in cyclonic vorticity (Figure 5a). Convection-related TIL (Figure 9e) and STR (Figure 9d) associated with divergence (Figure 5b) dominated this weakening, whereas other terms mainly acted in an opposite manner (Figures 9b, 9c and 9f). Overall, the vertical processes (VAV + TIL) were detrimental for the vortex’s development, and the horizontal processes (HAV + STR) mainly showed a neutral effect (Figures 9g and 9h).

In Period II (from 0000 UTC to 0900 UTC 20 July), term TOT mainly kept a strong positive value within the vortex’ vertical extent (Figure 9a), implying that conditions were favorable for the MCV’s development/sustainment. Horizontal transport (HAV; Figure 9b) and convection-related VAV (Figure 9c) were the dominant factors. For the former, it was mainly due to the vorticity transport within the central regions of the inverted trough over Henan (Figures 10a and 10b); for the latter, as shown in Figure 5a, cyclonic vorticity mainly increased downward;

Figure 7. Panel (a) illustrates the three-dimensional trajectories that featured cyclonic vorticity at the time when the mesoscale convective vortex (MCV) formed, where green dots mark the locations of the air particles 24-hr before the vortex’s formation, black dots mark the locations of the air particles when the vortex formed, shading represents relative humidity (RH; %), and the red number shows the proportion (relative to all the 567 trajectories) of these trajectories. Panel (b) is the same as panel (a) but for the trajectories that featured anticyclonic vorticity at the time when the MCV formed. Panels (c–e) show the variation in specific humidity (g kg^{-1}) of the trajectories in (a). Panels (f–h) show the variation in potential temperature (K) of the trajectories in panel (a). Panels (i–k) show the variation in height (m) of the trajectories in (a). Panels (l–n) show the variation in vorticity (10^{-5} s^{-1}) of the trajectories in panel (a). “Higher layer” means that the air particles came from the height higher than 4,000 m, “Middle layer” means that the air particles came from the height between 2,500 m and 4,000 m, “Lower layer” means that the air particles came from the height lower than 2,500 m, and the red number shows the proportion (relative to all the 567 trajectories) of corresponding trajectories.

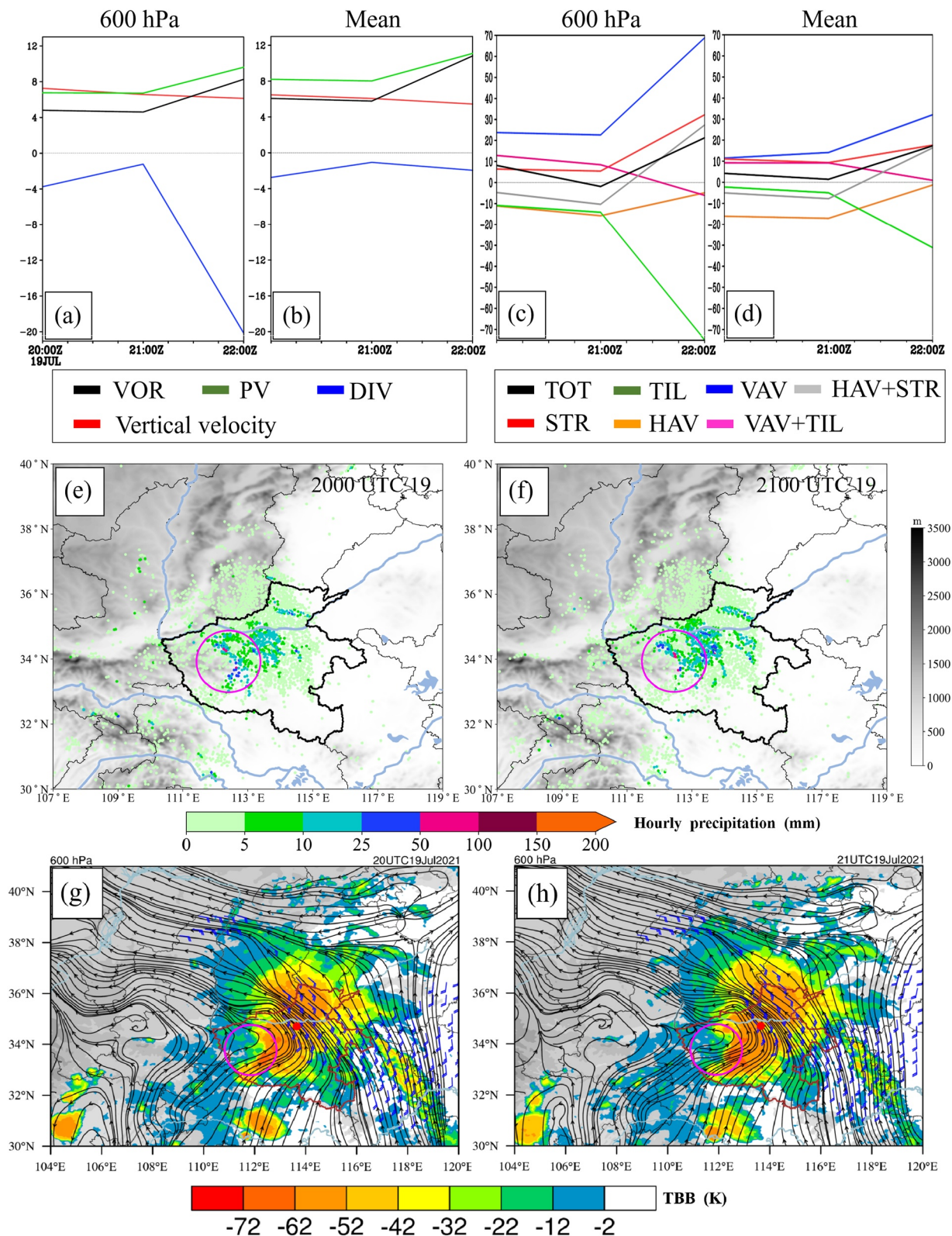


Figure 8.

therefore, ascending motions (Figure 5b) mainly transported stronger cyclonic vorticity upward, which rendered the strong VAV. It should be noted that the strong cyclonic vorticity beneath the bottom level of the MCV (Figure 5a), which was mainly produced by convergence (Figure 5b)-related vertical stretching (i.e., STR; Figure 9b), was of crucial importance for enhancing/maintaining the vortex around its bottom level (Figure 9c). In contrast, divergence-related vertical shrinking (Figure 9d) and tilting (Figure 9e) acted as the most detrimental factors for the upper (above 650 hPa) and lower (below 650 hPa) layers of the MCV, respectively. Overall, the vertical processes (VAV + TIL) and the horizontal processes (HAV + STR) dominated the vortex's development/sustainment in its upper and lower sections, respectively (Figures 9g and 9h).

During Period III (from 0900 UTC to 1200 UTC 20 July), term TOT weakened notably compared to that of Period II, implying that conditions became less favorable for the MCV's maintenance. Tilting changed to positive (Figure 9e), which acted as a dominant factor for sustaining the vortex. For comparison, it is clear that the strong negative TIL in the layer of 800–750 hPa kept negative from Period II to Period III, whereas for the layer of 600–550 hPa, the strong negative TIL changed to positive during the same period. Correspondingly, for the latter, its vertical wind shear (which could reflect the horizontal vorticity vector) changed much obviously than that of the former (cf., Figures 10c and 10d). This means that the change in vertical wind shears (as the MCV was decoupling from its parent MCS in this period) might be an important factor for the change in tilting. Horizontal import-transport of cyclonic vorticity was another favorable factor for the MCV's sustainment (Figure 9b), whereas other factors mainly acted conversely (Figures 9c, 9d and 9f). Overall, the vertical processes (VAV + TIL) contributed to the vortex's maintenance, whereas the horizontal processes (HAV + STR) mainly acted in an opposite manner (Figures 9g and 9h).

In Stage II, TOT weakened and changed to negative (Figure 9a), which finally rendered the MCV's dissipation. All vorticity budget terms weakened in their intensity as the vortex had already decoupled from its parent MCS (Figure 4b). Of all the terms, net-export horizontal transport (Figure 9b) dominated the vortex's decaying (Figure 9b), whereas vertical transport and tilting showed overall neutral effects (Figures 9c and 9e). As convergence dominated the vortex's vertical extent (Figure 5b), its associated vertical stretching (Figure 9d) served as the most important factor that decelerated the MCV's dissipation. Overall, both the vertical (VAV + TIL) and horizontal (HAV + STR) processes were mainly favorable for the vortex's sustainment before 1700 UTC 20 July (with the latter showing a more favorable effect), whereas after that, they both accelerated the vortex's dissipation (Figures 9g and 9h).

6. Conclusion and Discussion

The “21.7” TRE in Henan, which lasted from 17–22 July 2021, had broken a series of historical records, particularly for the extremely strong hourly precipitation of 201.9 mm at the Zhengzhou station, which was the largest hourly rainfall thus far observed by the meteorological observation stations over the Chinese Mainland. Sun et al. (2021) had concluded a series of factors that induced this TRE, of which a long-lived northward-moving MCV was a crucial feature. Although mesoscale vortices are frequently observed and acted as a key reason for TREs in China, the number of MCVs observed in China was small and thus needs more studies to enhancing the understanding of them. This study applied detailed analyses on the formation and evolution of the long-lived MCV during the “21.7” TRE and main findings are as follows: Table 2

1. The most intense precipitation of the “21.7” TRE appeared in the life span of the long-lived MCV (from 2200 UTC 19 to 1900 UTC 20 July 2021). It was a direct result of the interaction between the MCV and its parent MCS that covered Henan Province. During this period, the MCV and its parent MCS were dominated by a strong upper-level divergence ahead of an upper-tropospheric shortwave trough and a notable middle-level warm advection within the central region of a middle-tropospheric inverted trough. They were both favorable for enhancing/maintaining ascending motions. Heavy precipitation related to the MCV mainly appeared in its central and eastern sections as well as the regions east of it. Precipitation at the Zhengzhou station showed

Figure 8. Panel (a) shows the key-region averaged vorticity (VOR; 10^{-5} s^{-1}), divergence (DIV; 10^{-6} s^{-1}), potential vorticity (PV; 0.1 PVU , $1 \text{ PVU} = 10^{-6} \text{ K m}^{-2} \text{ kg}^{-1} \text{ s}^{-1}$), and vertical velocity (cm s^{-1}) at 600 hPa. Panel (b) is the same as panel (a) but for a vertical mean from 750 hPa to 600 hPa. Panel (c) shows the key-region averaged vorticity budget terms (10^{-10} s^{-2}) at 600 hPa. Panel (d) is the same as panel (c) but for a vertical mean from 750 to 600 hPa. Panels (e and f) are the hourly precipitation (shading dots; mm) at 2000 UTC and 2100 UTC 19 July, respectively. Panels (g and h) illustrate the temperature of the black body (temperature of black body; shading; K), stream field (black lines with arrows) and wind above 8 m s^{-1} (a full bar is 4 m s^{-1}) at 600 hPa, where big red dots mark the location of Zhengzhou. In panels (e–h), (m) gray shading represents terrain, and purple ellipses mark the central location of the mesoscale convective vortex when it is formed.

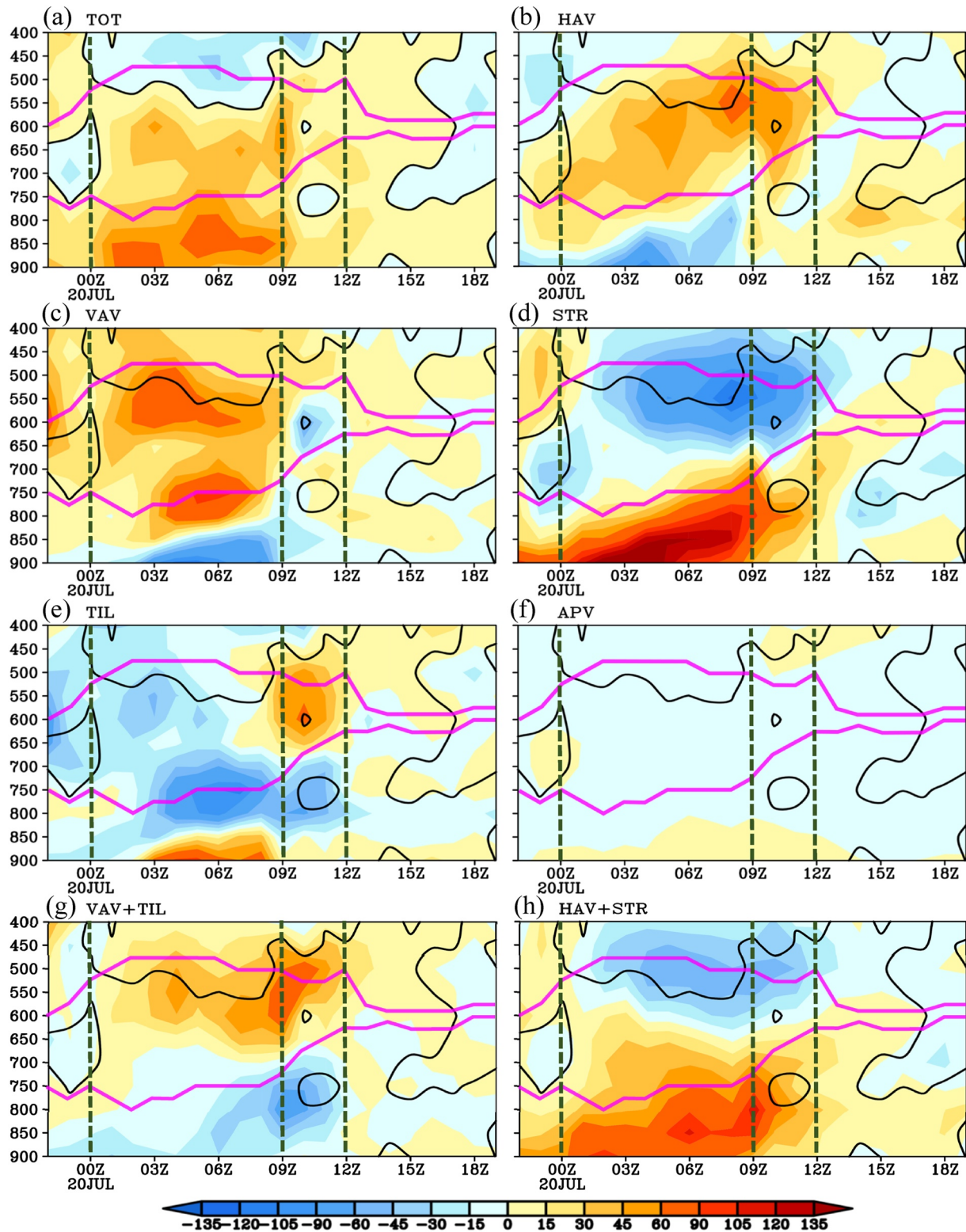


Figure 9. Panels (a–h) show total effect term (TOT), horizontal advection of vorticity (HAV), vertical advection of vorticity (VAV), stretching effect (STR), tilting effect (TIL), advection of planet vorticity, VAV + TIL, and HAV + STR (shading, units: 10^{-10} s^{-2}), respectively, where the black contours outline the zero value of TOT. Thick purple lines are the top and bottom levels of the mesoscale convective vortex (MCV), respectively. Thick dashed green lines mark typical stages of the MCV.

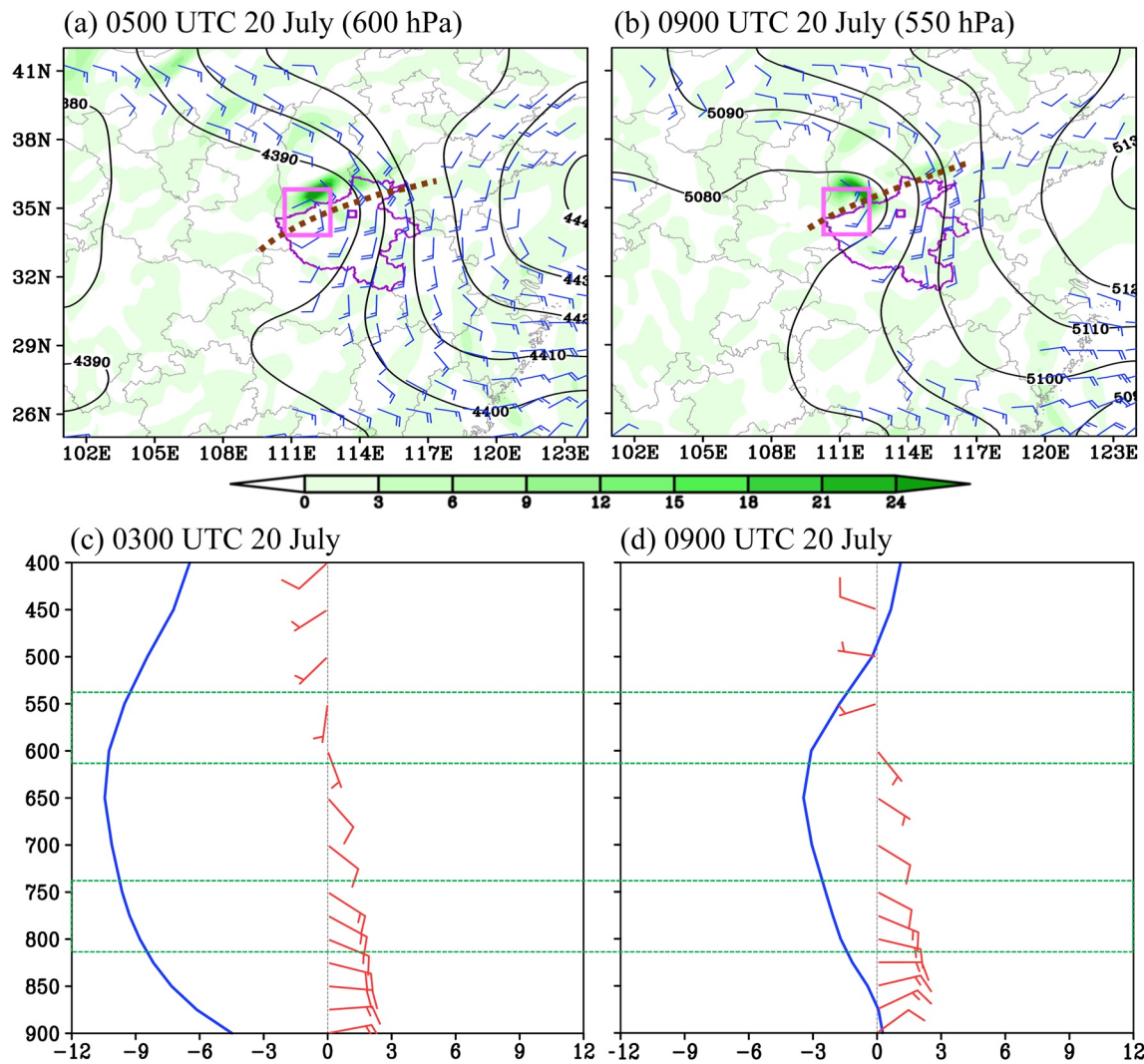


Figure 10. Panels (a and b) show term horizontal advection of vorticity (shading; 10^{-9} s^{-2}), geopotential height (black contour; gpm), and wind above 5 m s^{-1} (a full bar is 5 m s^{-1}) at typical levels in typical stages, where the purple box marks the mesoscale convective vortex's key region and thick dashed brown lines are the trough lines. Panels (c and d) show key-region averaged horizontal wind vector (a full bar is 5 m s^{-1}) and vertical motions (blue line; $10^{-1} \text{ Pa s}^{-1}$) during typical stages, where thin dashed lines mark two typical layers.

Table 2

The Sign of the Term Total Effect Term ("Neutral" Means Close to Zero) as Well as the Favorable and Detrimental Factors for the Mesoscale Convective Vortex's Development/Maintenance in Terms of the Vorticity Budget

	Stage I			Stage II
	Period I	Period II	Period III	
TOT	Negative	Positive	Positive	Neutral
Favorable factors	VAV; HAV; APV	VAV; HAV	TIL; HAV	STR
Detrimental factors	<i>TIL; STR</i>	<i>STR; TIL; APV</i>	<i>STR; VAV; APV</i>	<i>HAV; VAV; TIL; APV</i>

Note. Dominant factors are highlighted in bold, and the most detrimental factor is highlighted in italic. Period I: from 2200 UTC 19 to 0000 UTC 20 July; Period II: from 0000 UTC to 0900 UTC 20 July; Period III: from 0900 UTC to 1200 UTC 20 July; Stage I: Period I + Period II + Period III; Stage II: 1200 UTC–1900 UTC 20 July.

consistent variations with the MCV's intensity (which was strong when the MCV and its parent MCS coupled with each other, whereas it weakened sharply after the MCV decoupled from the MCS). Strong ascending motions (mainly due to convection-related latent heat release) and southerly winds associated with the MCV were key mechanisms of how the MCV contributed to the extremely strong hourly rainfall of 201.9 mm at the Zhengzhou station.

2. The MCV lasted for a life span of 21 hr and mainly moved in the northwest direction due to the steering of the southeasterly wind associated with the inverted trough in the background environment. The vortex was mainly located in the middle and lower troposphere (the thickest vertical extent was 800–475 hPa) with its thickness much thicker when it coupled with its parent MCS than that after it decoupled from the MCS. Air particles originated from the lower layer made the largest contribution (~76.2%) to the MCV's formation. These air particles experienced notable ascending motions and condensation as most of them came from the region east of the MCV, which was directly affected by the parent MCS. Air particles from the middle layer made the second contribution (~21%) with most of them originated from the region southwest of the vortex, where convection was relatively weak.
3. The 1-hr period before the MCV's formation was of crucial importance to the vortex's generation, as the cyclonic vorticity associated with the MCV was mainly produced in this period. Strong upward transport of cyclonic vorticity and convergence-related vertical stretching, both of which were mainly due to intense convection associated with the parent MCS, acted as the most and second most favorable factors for the MCV's formation. Mechanisms governing the MCV's variation during different stages were summarized in Table 2. For the period when the MCV coupled with its parent MCS (Period I and Period II), convection-related upward transport of cyclonic vorticity and net-import horizontal transport of cyclonic vorticity associated with the inverted trough dominated the vortex's development/maintenance; for the period when the MCV began to decouple from its parent MCS, tilting and horizontal transport governed the vortex's sustainment; for the period when the MCV completely decoupled from the MCS, net-export horizontal transport dominated its dissipation.

The MCV was only one of the key factors that produced the extremely strong hourly precipitation in Zhengzhou. Based on high-resolution simulations, Yin et al. (2022) supposed a possible dynamic mechanism for the extremely strong hourly rainfall: the arc-shaped convergence zone associated with an intense quasi-stationary, well-organized meso- γ -scale convective system served as “multidirectional lifting pumps,” which transported precipitation from different regions into Zhengzhou, and thus produced the extreme rainfall. This arc-shaped convergence zone was closely related to the MCV discussed in this study. Compared to the general features documented in statistical studies on MCVs (Bartels & Maddox, 1991; James & Johnson, 2010; Trier et al., 2000), the MCV in this article was typical in its diameter, thickness, intensity, and formation time, but longer in life span (i.e., 21 hr). Compared with the various mechanisms that favored MCVs' formation/sustainment (e.g., Clark et al., 2010; Cram et al., 2002; Davis & Galarneau, 2009; Galarneau et al., 2009; Kirk, 2003, 2007; Knievel & Johnson, 2003; Sun et al., 2010; D.-L. Zhang, 1992), the most distinctive feature for the MCV in this event was that the horizontal advection acted as a dominant factor, whereas the term STR (i.e., divergence-related vertical shirking) mainly served as a detrimental factor. Differences in the background environment were an important reason for the differences in mechanisms. Another feature worth mentioning is that there was a decoupling process of the MCV from its parent MCS (which was still strong in intensity) in this event, which was absent in many previous studies (e.g., Bartels et al., 1996; Clark et al., 2010; Fritsch et al., 1994; Trier & Davis, 2007). Compared to the much more active mesoscale vortices in China (e.g., TPVs, SWVs, and DBVs), the MCV was similar in thickness (Curio et al., 2018; Fu et al., 2015, 2017; Ni et al., 2017; Tang et al., 2020; Yang et al., 2010; J.-P. Zhang et al., 2015; Zhao & Fu, 2007), but much smaller in diameter. Governing mechanisms of them were notably different as the convergence-related vertical stretching was the dominant factor for most of TPVs, SWVs, and DBVs.

As the cyclonic vorticity associated with the MCV was mainly produced within 1-hr before the vortex's formation, in the future, we will carry out high-resolution (in both temporal and spatial resolution) numerical simulation studies on this particularly important period. After successfully reproduced the MCV during the “21.7” TRE, by using dynamical diagnoses (e.g., vorticity and circulation budgets), we can explore more information about the MCV's formation.

Data Availability Statement

The hourly precipitation observations at meteorological stations from the China Meteorological Administration are available at <http://data.cma.cn/en/?r=data/detail&dataCode=A.0012.0001>. The ERA5 reanalysis data (<https://cds.climate.copernicus.eu/cdsapp#!/dataset/reanalysis-era5-pressure-levels?tab=overview>; DOI: 10.24381/cds.bd0915c6) are introduced in Hersbach et al. (2020). The temperature of black body data from the FY-IV satellite are openly available at <http://satellite.nsmc.org.cn/PortalSite/Data/Satellite.aspx>. The HYSPLIT model can be downloaded at <https://www.ready.noaa.gov/HYSPLIT.php> and is introduced in Stein et al. (2015).

Acknowledgments

This research was supported by the National Natural Science Foundation of China (Grant Nos. U2142202 and 42075002), the Open Grants of the State Key Laboratory of Severe Weather (Grant No. 2021LASW-A10), and the National Key Scientific and Technological Infrastructure Project “Earth System Science Numerical Simulator Facility”.

References

- Bartels, D. L., Brown, J. M., & Tollerud, E. I. (1996). Structure of a midtropospheric vortex induced by a mesoscale convective system. *Monthly Weather Review*, 125(2), 193–211. [https://doi.org/10.1175/1520-0493\(1997\)125<0193:soamvi>2.0.co;2](https://doi.org/10.1175/1520-0493(1997)125<0193:soamvi>2.0.co;2)
- Bartels, D. L., & Maddox, R. A. (1991). Midlevel cyclonic vortices generated by mesoscale convective systems. *Monthly Weather Review*, 119(1), 104–118. [https://doi.org/10.1175/1520-0493\(1991\)119<0104:mcvghm>2.0.co;2](https://doi.org/10.1175/1520-0493(1991)119<0104:mcvghm>2.0.co;2)
- Carissimo, B. R., Pierrehumbert, R. T., & Pham, H. L. (1988). An estimate of mountain drag 253 during ALPEX for comparison with numerical models. *Journal of the Atmospheric Sciences*, 45(13), 1949–1960. [https://doi.org/10.1175/1520-0469\(1988\)045<1949:aomdd>2.0.co;2](https://doi.org/10.1175/1520-0469(1988)045<1949:aomdd>2.0.co;2)
- Clark, A. J., Gallus, W. A., Jr., Xue, M., & Kong, F. (2010). Convection-allowing and convection-parameterizing ensemble forecasts of a mesoscale convective vortex and associated severe weather environment. *Weather and Forecasting*, 25(4), 1052–1081. <https://doi.org/10.1175/2010Waf2222390.1>
- Cram, T. A., Montgomery, M. T., & Hertenstein, R. F. A. (2002). Early evolution of vertical vorticity in a numerically simulated idealized convective line. *Journal of the Atmospheric Sciences*, 59(13), 2113–2127. [https://doi.org/10.1175/1520-0469\(2002\)059<2113:eeovvi>2.0.co;2](https://doi.org/10.1175/1520-0469(2002)059<2113:eeovvi>2.0.co;2)
- Curio, J., Chen, Y., Schiemann, R., Turner, A. G., Wong, K. C., Hodges, K., & Li, Y. (2018). Comparison of a manual and an automated tracking method for Tibetan Plateau vortices. *Advances in Atmospheric Sciences*, 35(8), 965–980. <https://doi.org/10.1007/s00376-018-7278-4>
- Curio, J., Schiemann, R., Hodges, K. I., & Turner, A. G. (2019). Climatology of Tibetan Plateau vortices in reanalysis data and a high-resolution global climate model. *Journal of Climate*, 32(6), 1933–50. <https://doi.org/10.1175/jcli-d-18-0021.1>
- Davis, C. A., & Galarneau, T. J., Jr. (2009). The vertical structure of mesoscale convective vortices. *Journal of the Atmospheric Sciences*, 66(3), 686–704. <https://doi.org/10.1175/2008jas2819.1>
- Feng, S.-L., Jin, S.-L., Fu, S.-M., Sun, J.-H., & Zhang, Y.-C. (2019). Formation of a kind of heavy-rain-producing mesoscale vortex around the Sichuan basin: An along-track vorticity budget analysis. *Atmospheric Science Letters*, 21(1), e949. <https://doi.org/10.1002/asl2.949>
- Feng, X., Liu, C., Rasmussen, R., & Fan, G. (2014). A 10-yr climatology of Tibetan Plateau vortices with NCEP climate forecast system reanalysis. *Journal of Applied Meteorology and Climatology*, 53(1), 34–46. <https://doi.org/10.1175/jamc-d-13-014.1>
- Fritsch, J. M., Murphy, J. D., & Kain, J. S. (1994). Warm core vortex amplification over land. *Journal of the Atmospheric Sciences*, 51(13), 1780–1807. [https://doi.org/10.1175/1520-0469\(1994\)051<1780:wcvao1>2.0.co;2](https://doi.org/10.1175/1520-0469(1994)051<1780:wcvao1>2.0.co;2)
- Fu, S.-M., Li, W.-L., Sun, J.-H., Zhang, J.-P., & Zhang, Y.-C. (2015). Universal evolution mechanisms and energy conversion, characteristics of long-lived mesoscale vortices over the Sichuan Basin. *Atmospheric Science Letters*, 16(2), 127–34. <https://doi.org/10.1002/asl2.533>
- Fu, S.-M., Mai, Z., Sun, J.-H., Li, W.-L., Ding, Y., & Wang, Y.-Q. (2019). Impacts of convective activity over the Tibetan Plateau on plateau vortex, southwest vortex, and downstream precipitation. *Journal of the Atmospheric Sciences*, 76(12), 3803–3830. <https://doi.org/10.1175/jas-d-18-0331.1>
- Fu, S.-M., Sun, J.-H., Luo, Y.-L., & Zhang, Y.-C. (2017). Formation of long-lived summertime mesoscale vortices over central east China: Semi-idealized simulations based on a 14-year vortex statistic. *Journal of the Atmospheric Sciences*, 74(12), 3955–3979. <https://doi.org/10.1175/jas-d-16-0328.1>
- Fu, S.-M., Zhang, J.-P., Sun, J.-H., & Zhao, T.-B. (2016). Composite analysis of long-lived mesoscale vortices over the middle reaches of the Yangtze River valley: Octant features and evolution mechanisms. *Journal of Climate*, 29(2), 761–781. <https://doi.org/10.1175/jcli-d-15-0175.1>
- Galarneau, T. J., Jr., Bosart, L. F., Davis, C. A., & McTaggart-Cowan, R. (2009). Baroclinic transition of a long-lived mesoscale convective vortex. *Monthly Weather Review*, 137(2), 562–584. <https://doi.org/10.1175/2008mwr2651.1>
- Hersbach, H., Bell, B., Berrisford, P., Hirahara, S., Horanyi, A., Munoz-Sabater, J., et al. (2020). The ERA5 global reanalysis. *Quarterly Journal of the Royal Meteorological Society*, 146(730), 1999–2049. <https://doi.org/10.1002/qj.3803>
- Holton, J. R. (2004). *An introduction to dynamic meteorology* (p. 552pp). Academic Press.
- James, E. P., & Johnson, R. H. (2010). A climatology of midlatitude mesoscale convective vortices in the rapid update cycle. *Monthly Weather Review*, 138(5), 1940–1956. <https://doi.org/10.1175/2009mwr3208.1>
- Kirk, J. R. (2003). Comparing the dynamical development of two mesoscale convective vortices. *Monthly Weather Review*, 131(5), 862–890. [https://doi.org/10.1175/1520-0493\(2003\)131<0862:ctddot>2.0.co;2](https://doi.org/10.1175/1520-0493(2003)131<0862:ctddot>2.0.co;2)
- Kirk, J. R. (2007). A phase-plot method for diagnosing vorticity concentration mechanisms in mesoscale convective vortices. *Monthly Weather Review*, 135(3), 801–820. <https://doi.org/10.1175/mwr3322.1>
- Knievel, J. C., & Johnson, R. H. (2003). A scale-discriminating vorticity budget for a mesoscale vortex in a midlatitude, continental convective system. *Journal of the Atmospheric Sciences*, 60(6), 781–794. [https://doi.org/10.1175/1520-0469\(2003\)060<0781:asdvbf>2.0.co;2](https://doi.org/10.1175/1520-0469(2003)060<0781:asdvbf>2.0.co;2)
- Mai, Z., Fu, S.-M., Sun, J.-H., Hu, L., & Wang, X.-M. (2020). Key statistical characteristics of the mesoscale convective systems generated over the Tibetan Plateau and their relationship to precipitation and southwest vortices. *International Journal of Climatology*, 36(S1), 3148–3160. <https://doi.org/10.1002/joc.6735>
- Ni, C.-C., Li, G.-P., & Xiong, X.-Z. (2017). Analysis of a vortex precipitation event over southwest China using AIRS and in situ measurements. *Advances in Atmospheric Sciences*, 34(4), 559–570. <https://doi.org/10.1007/s00376-016-5262-4>
- Orlanski, I. (1975). A rational subdivision of scales for atmospheric processes. *Bulletin of the American Meteorological Society*, 56, 527–530. Retrieved from <https://www.jstor.org/stable/26216020>
- Raymond, D., & Jiang, H. (1990). A theory for long-lived mesoscale convective systems. *Journal of the Atmospheric Sciences*, 47(24), 3067–3077. [https://doi.org/10.1175/1520-0469\(1990\)047<3067:atflm>2.0.co;2](https://doi.org/10.1175/1520-0469(1990)047<3067:atflm>2.0.co;2)
- Song, L. C. (2018). *Yearbook of meteorological disasters in China* (p. 229). China Meteorological Press.
- Stein, A. F., Draxler, R. R., Rolph, G. D., Stunder, B. J. B., Cohen, M. D., & Ngan, F. (2015). NOAA'S HYSPLIT atmospheric transport and dispersion modeling system. *Bulletin American Meteorology Social*, 96(12), 2059–2077. <https://doi.org/10.1175/bams-d-14-00110.1>

- Sun, J.-H., Wang, H., Fu, S., & Zhang, Y. (2021). Primary characteristics of the extremely heavy rainfall event over Henan in July 2021. *Advances in Atmospheric Sciences*, 38(12), 2167–2182. <https://doi.org/10.1007/s00376-021-1194-8>
- Sun, J.-H., Zhao, S.-X., Xu, G.-K., & Meng, Q.-T. (2010). Study on a mesoscale convective vortex causing heavy rainfall during the Mei-yu Season in 2003. *Advances in Atmospheric Sciences*, 27(5), 1193–1209. <https://doi.org/10.1007/s00376-009-9156-6>
- Surowiecki, A., & Taszarek, M. (2020). A 10-year radar-based climatology of mesoscale convective system archetypes and derechos in Poland. *Monthly Weather Review*, 148(8), 3471–3488. <https://doi.org/10.1175/mwr-d-19-0412.1>
- Tang, H., Fu, S.-M., Sun, J.-H., Mai, Z., Jin, S.-L., & Zhang, Y.-C. (2020). Investigation of severe precipitation event caused by an eastward-propagating MCS originating from the Tibetan Plateau and a downstream southwest vortex. *Chinese Journal of Atmospheric Sciences*, 44, 1275–1290.
- Tao, S.-Y. (1980). *Rainstorms in China* (p. 225pp). Science Press.
- Trier, S. B., & Davis, C. A. (2007). Mesoscale convective vortices observed during BAMEX. Part II: Influences on secondary deep convection. *Monthly Weather Review*, 135(6), 2051–2075. <https://doi.org/10.1175/mwr3399.1>
- Trier, S. B., Davis, C. A., & Tuttle, J. D. (2000). Long-lived mesoconvective vortices and their environment. Part I: Observations from the central United States during the 1998 warm season. *Monthly Weather Review*, 128(10), 3376–3395. [https://doi.org/10.1175/1520-0493\(2000\)128<3376:llmvtat>2.0.co;2](https://doi.org/10.1175/1520-0493(2000)128<3376:llmvtat>2.0.co;2)
- Tutis, V., & Ivancan-Picek, B. (1991). Pressure drag on the Dinaric Alps during the ALPEX SOP. *Meteorology and Atmospheric Physics*, 47(1), 73–81. <https://doi.org/10.1007/bf01025829>
- Yang, Y.-M., Gu, W.-L., Zhao, R.-L., & Liu, J. (2010). The statistical analysis of low vortex during Meiyu season in the lower reaches of the Yangtze. *Appl. Meteor. Sci.*, 21, 11–18.
- Yin, J.-F., Gu, H.-D., Liang, X.-D., Yu, M., Sun, J.-S., Xie, Y.-X., et al. (2022). A possible dynamic mechanism for rapid production of the extreme hourly rainfall in Zhengzhou City on 20 July 2021. *J. Meteor. Res.*, 36, 1–20. <https://doi.org/10.1007/s13351-022-1166-7>
- Yu, S.-H., & Gao, W.-L. (2006). Observational analysis on the movement of vortices before/after moving out the Tibetan Plateau. *Acta Meteorologica Sinica*, 64, 92–399.
- Zhang, D.-L. (1992). The formation of a cooling-induced mesovortex in the trailing stratiform region of a midlatitude squall line. *Monthly Weather Review*, 120(12), 2763–2785. [https://doi.org/10.1175/1520-0493\(1992\)120<2763:tfoaci>2.0.co;2](https://doi.org/10.1175/1520-0493(1992)120<2763:tfoaci>2.0.co;2)
- Zhang, J.-P., Fu, S.-M., Sun, J.-H., Shen, X.-Y., & Zhang, Y.-C. (2015). A statistical and compositional study on the two types of mesoscale vortices over the Yangtze River Basin. *Climatic and Environmental Research*, 20, 319–336.
- Zhao, S.-X., & Fu, S.-M. (2007). An analysis on the southwest vortex and its environment fields during heavy rainfall in eastern Sichuan Province and Chongqing in September 2004. *Chinese Journal of Atmospheric Sciences*, 31, 1059–1075.
- Zhao, S.-X., Tao, Z. Y., Sun, J. H., & Bei, N. F. (2004). *Study on mechanism of formation and development of heavy rainfalls on meiyu front in Yangtze River* (p. 282pp). China Meteorological Press.